Ocean Modelling 179 (2022) 102109

Contents lists available at ScienceDirect

Ocean Modelling

journal homepage: www.elsevier.com/locate/ocemod

TIMCOM model datasets for the CMIP6 Ocean Model Intercomparison Project

Yu-Heng Tseng [a,b,*], Shou-En Tsao [a], Yi-Chun Kuo [a], Jia-Ying Tsai [a]

[a] Institute of Oceanography, National Taiwan University, Taiwan
[b] Ocean Center, National Taiwan University, Taiwan

ARTICLE INFO

Keywords:
Ocean–sea ice model
CMIP6
OMIP
TIMCOM
AMOC increase

ABSTRACT

The participation of the Taiwan Multi-scale Community Ocean Model (TIMCOM) in the Ocean Model Intercomparison Project (OMIP) experiments is introduced here, as part of phase 6 of the Coupled Model Intercomparison Project (CMIP6). Two ocean–sea ice model experiments are compared: (a) OMIP1, forced by the Coordinated Ocean-Ice Reference Experiments Phase II data (1948–2009), and (b) OMIP2, forced by JRA55-do data (1958–2018). The observed annual means and the interannual variability of physical states are reasonably captured in both experiments, but improved mean temperatures and salinities are found in OMIP2. The weaker winds and stronger freshwater discharge in the OMIP2 forcing contribute to some simulated differences between OMIP1 and OMIP2. Many patterns and biases are similar to those found in other modeling efforts, confirming the common systematic biases. However, a few unique features are found in this study, including the recent increase of the Atlantic Meridional Overturning Circulation (AMOC) that has been observed in the last decade and a generally higher Drake Passage transport. The enhanced AMOC can be explained by the recent cooling event over the North Atlantic, which thermally increased the surface density flux. The higher Drake Passage transport compared to observations is possibly linked to a stronger bottom cell of meridional circulation and a smaller Antarctic sea-ice extent.

1. Introduction

The ocean is an important component within the Earth system. The large water mass of the global ocean makes it a major reservoir for heat and carbon storage. Ocean general circulation models (OGCMs) have greatly advanced in the last few decades; they can simulate long-term global ocean changes. This has improved our understanding of the global ocean's mean status and its related climate variability. OGCMs also make it possible to predict the future ocean state under assumed future scenarios (e.g., Hemer et al., 2013). Nevertheless, large inter-model spreads in simulation results exist across different time scales. In the recent phase 6 of the Coupled Model Intercomparison Project (CMIP6) (Eyring et al., 2016), the Ocean Model Intercomparison Project (OMIP) was proposed to trace the systematic biases within the coupled model that might originate from the ocean–sea ice model (Griffies et al., 2016). The OMIP provides a standardized experimental protocol for ocean–sea ice simulations forced with common atmospheric datasets.

Two different atmospheric datasets are used in the OMIP protocol. Phase 1 of OMIP (OMIP1) is forced by the Coordinated Ocean-Ice Reference Experiments-II (CORE-II, Griffies et al., 2009) dataset (Large and Yeager, 2009), which is mainly derived from the National Center for Environmental Prediction-National Center for Atmospheric Research (NCEP–NCAR) atmospheric reanalysis (Kistler et al., 2001) and covers a period of 62 years (1948–2009). The CORE-II framework has served as a common platform for many comprehensive assessments of ocean–sea ice models (e.g., Danabasoglu et al., 2014, 2016; Griffies et al., 2014; Farneti et al., 2015; Tseng et al., 2016b). Recently, to update the forcing dataset and improve the infrastructural design of experiments, Phase 2 of OMIP (OMIP2) was designed; in this phase, the ocean model is forced by the JRA55-do dataset (Tsujino et al., 2018). This dataset is based on the Japanese 55 year reanalysis (JRA-55) dataset (Kobayashi et al., 2015), which covers a period from 1958–2018 and receives incremental updates with time. Compared with CORE-II, the JRA55-do forcing has an increased temporal frequency (from 6 to 3 h) and a refined horizontal resolution (from 1.875 to 0.5625°). It also has the advantage of self-consistency compared to the previous CORE-II effort because it incorporates various atmosphere fields and river runoff into a single reanalysis dataset.

A recent comparison study compiled results from 11 international modeling groups involved in the OMIP1 and OMIP2 experiments (Tsujino et al., 2020). Some improvements resulting from the use of the OMIP2 forcing data have been clearly identified, such as the reduction in warm biases off the eastern coast of the Pacific Ocean and better

* Corresponding author at: Institute of Oceanography, National Taiwan University, Taiwan.
E-mail address: tsengyh@ntu.edu.tw (Y.-H. Tseng).

https://doi.org/10.1016/j.ocemod.2022.102109
Received 5 February 2022; Received in revised form 9 August 2022; Accepted 29 August 2022
Available online 13 September 2022

sea surface temperature (SST) changes (e.g., warming hiatus pattern after 2000). However, there are also common biases across each individual model when they are compared to observations, suggesting systematic errors within the model representations or unresolved key dynamical processes. The reduction of the biases of the multi-model mean represents a current ocean modeling challenge; these biases may be caused by the limitations of the horizontal resolution (e.g., poorly resolved coastal upwelling, eddy-rich regions, and narrow straits) and in other cases by errors in the atmospheric forcing. Some key improvements have been shown by the high-horizontal-resolution ($\sim 0.1°$) models (Chassignet et al., 2020); however, the inconsistency of the improvements across different model families suggests that resolution refinement does not necessarily improve the biases in all regions for all high-resolution models. The sources of model biases across different model configurations have not yet been explored. Recently, based on a single model framework (CAS-LICOM), Li et al. (2020) suggested that a finer eddy-resolving resolution can greatly enhance the robustness of large-scale SST patterns (Lin et al., 2020; Dong et al., 2021). They found that this enhancement occurs due to the improved eddy transfer process; however, systematic biases persisted in sea surface salinity (SSS), possibly due to biases in the surface water flux. These findings allow us to further assess the origin of coupled model biases, which may or may not be dependent on the resolution, a computationally limited factor.

Here, we present results from the newly revised Taiwan Multi-scale Community Ocean Model (TIMCOM) to make a contribution to the OMIP protocol. Many of the model biases are comparable to other modeling results described in Tsujino et al. (2020), while others are unique, providing possible insights for inter-model comparisons. A baseline evaluation of TIMCOM using OMIP1 and OMIP2 experiments is performed to assess the model quality. Systematic and model-dependent errors can be better clarified through this evaluation. We structure this paper in the following way: Section 2 describes the model and experiment design; Section 3 presents our model validation for the OMIP1 and OMIP2 experiments; and Section 4 addresses the recent increase of the Atlantic Meridional Overturning Circulation (AMOC) starting in 2010. Finally, a discussion and summary are provided in Section 5.

2. Model and experiments

2.1. Model details

TIMCOM is an easy-to-use community ocean model that has been used in many regional and global applications (Tseng and Chien, 2011; Tseng et al., 2012; Young et al., 2012; Tseng et al., 2016b). The global ocean–sea ice coupled TIMCOM configuration is built within the Taiwan Earth System Model framework (Lee et al., 2020).

The ocean–sea ice global TIMCOM domain extends from 86°S to 86°N. A symmetric boundary condition is imposed at the northern boundary rather than using the common displaced-pole grid approach (e.g., exchanging the lateral boundary condition between 90°E and 90°W). Therefore, the North Pole is treated as an infinitely small circle that can freely exchange the northern boundary condition across the pole. TIMCOM applies a fourth-order-accurate spatial discretization to the combined Arakawa A- and C-grids. The grid resolution is 320×288. A fixed 1.125° resolution is used zonally and a varying resolution is used meridionally; it linearly varies from approximately 0.3° at the equator to about 0.9° at high latitudes. The vertical grid is based on a z-level coordinate. It is a linear-exponentially stretched grid of 55 levels with a thickness ranging from roughly 10 m at the top to 500 m in the abyssal ocean.

The vertical mixing is based on the K-profile parameterization (Large et al., 1994) with a critical Richardson number of 0.3, and it has a latitudinally varying background internal wave diffusivity that is calculated according to Danabasoglu et al. (2006). The Gent–McWilliams (GM) parameterization (Gent and Mcwilliams, 1990), replacing the horizontal diffusion of tracers with advective plus isopycnal diffusion, resolves tracer mixing by mesoscale eddies on isopycnal surfaces in coarse-resolution ocean models. This GM parameterization is included in the latest global TIMCOM. Here, we set the maximum slopes for the (Redi, 1982) isopycnal diffusion terms to 0.3. The background diffusivity is based on the vertical location with respect to the diabatic, transition, and adiabatic regions. In the surface diabatic layer, the horizontal diffusivity coefficient is set to 3000 $m^2\ s^{-1}$. The diffusivity decreases with depth and vanishes at the seafloor. In addition, abyssal tidal mixing parameterization is used to represent the deep vertical mixing arising from the breaking of tidally-generated internal waves over rough topography (St. Laurent and Garrett, 2002; Jayne, 2009). The viscous and quadratic bottom drag is also included.

The model is integrated using a modified Robert–Asselin–Williams filtered leapfrog scheme with a time step of 8 min (Williams, 2009; Young et al., 2014). The small time step is mainly due to the required Courant–Friedrichs–Lewy condition in the Arctic. Finally, for the sea ice component, TIMCOM uses the Los Alamos sea ice model version 4 (CICE4; Hunke et al., 2008), which is fully thermodynamical and operates on the same horizontal grid as the ocean with a time step of 1 h.

2.2. OMIP experiments

As part of our participation in the CMIP6-OMIP, to assess the quality of our global ocean sea-ice coupled model, we conduct two experiments following the OMIP1 and OMIP2 protocols; see Tsujino et al. (2020) for more interannual forcing details. OMIP1 is integrated from 1948–2009 (62 years) based on CORE-II forcing (Large and Yeager, 2009), while OMIP2 is integrated from 1958–2018 (61 years) based on JRA55-do forcing (Tsujino et al., 2018). Both experiments have been run for six cycles. The temperature and salinity are initialized from the Polar Science Center Hydrographic Climatology version 2 (PHC2) observations (Steele et al., 2001). The sea-surface salinity in both experiments is restored to the monthly PHC2, with a salinity restoring time of 90 days for 10 m to ensure a fair comparison between OMIP1 and OMIP2.

Common observations are used for model validation. Annual means of the SST and Sea Ice Concentration (SIC) are acquired from HadISST (Hadley Centre Sea Ice and Sea Surface Temperature dataset; https://www.metoffice.gov.uk/hadobs/hadisst/) (Rayner et al., 2003). The observed sea surface height (SSH) is taken from AVISO (Archiving, Validation and Interpretation of Satellite Oceanographic Data; http://www.aviso.altimetry.fr/). The annual mean ocean temperature and salinity based on the World Ocean Atlas 13 (WOA13) (Locarnini et al., 2013; Zweng et al., 2013) are used for further comparison. The observed vertical profiles of the time-averaged AMOC at 26.5 °N are taken from the data of RAPID (Rapid Climate Change) program (Smeed et al., 2018).

3. General features

3.1. Global mean time series

The global annual mean temperature and salinity at the surface (SST, SSS) and for the whole ocean volume (mean T, mean S) over the completed six cycles are shown in Fig. 1 to evaluate the impacts of model spin-up. There are 372 and 366 years of data for the OMIP1 (1948–2009) and OMIP2 (1958–2018) experiments, respectively. The cyclic features and interannual variation are relatively clear in the global mean SST and SSS, which periodically repeat throughout each cycle, ranging roughly from 18.0–18.4 °C and 34.6–34.7 psu, respectively. The global mean SST and SSS during the last cycle are 18.4 °C and 34.7 psu, respectively. The global volume-averaged ocean temperature (mean T) and salinity (mean S) become relatively stationary

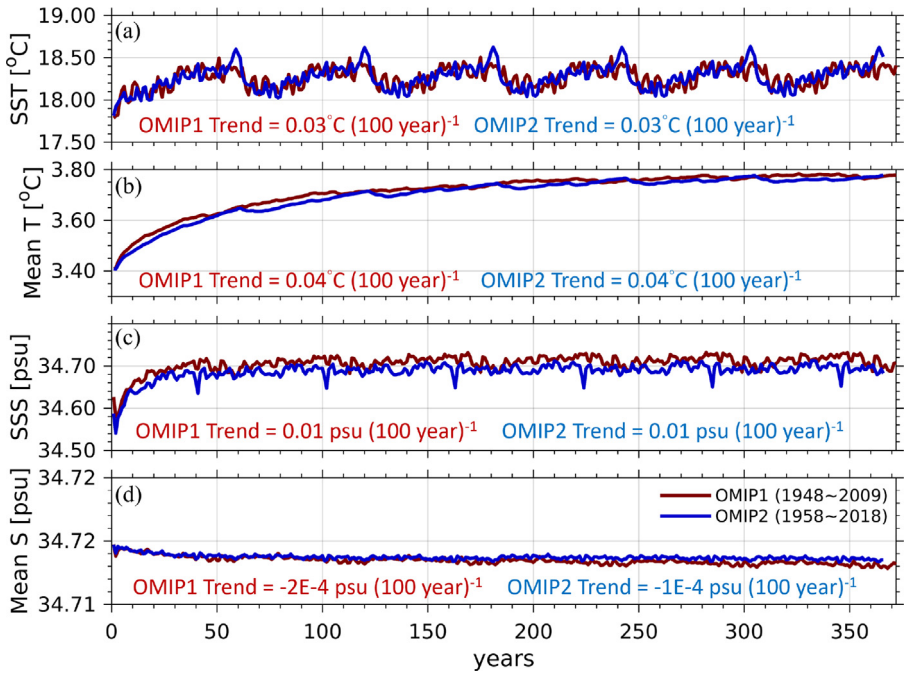

Fig. 1. Time series of global annual mean of (a) SST, (b) volume-averaged temperature, (c) SSS, and (d) volume-averaged salinity for OMIP1 (red) and OMIP2 (blue) experiments over six cycles.

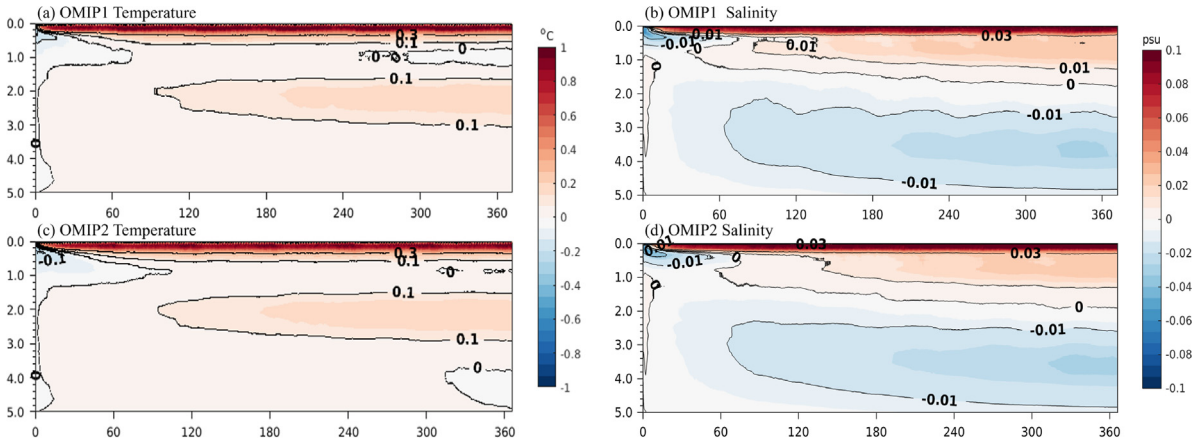

Fig. 2. Time series of drifted horizontal mean (a) OMIP1 temperature (°C), (b) OMIP1 salinity (psu), (c) OMIP2 temperature (°C), and (d) OMIP2 salinity (psu) as a function of depth (km) and time (years). The drift is defined as the deviation from the global annual mean of the initial year.

after the fourth cycle, suggesting that the model has reached a quasi-equilibrium state. Over all six cycles, the global SST and SSS show slightly increasing trends of 0.03 °C per century and 0.01 psu per century, respectively, while the volume-averaged mean T and S are relatively stable, especially after the fourth cycle.

Fig. 2 presents the drifts of the globally averaged horizontal temperature and salinity in terms of the deviation from the initial year. Our model shows an increasing temperature drift with time for the whole water column, with the largest drift near the upper 500 m. In addition to the upper ocean warming drift, the other strong warming trend occurs at a water depth of around 2 km. This is consistent with the inter-model comparison study of Tsujino et al. (2020) (see Figs. 2 and 3 in their paper). All models agree on the increasing temperature drift in the upper ocean, but the models disagree at deep to bottom sub-surface depths. A large spread with a decreasing multi-model mean exists in the deep ocean. The drifts in our OMIP1 and OMIP2 experiments show a very similar trend, with more evident changes after the fifth cycle (Fig. 2a, c), suggesting very similar model drift characteristics with different atmospheric forcing responses after long-term integration.

In terms of the salinity (Fig. 2b, d), the upper ocean saltening and deep ocean freshening appear in both the OMIP1 and OMIP2 experiments with similar behaviors. This feature is consistent with the multi-model mean in Tsujino et al. (2020). The drifted changes of temperature and salinity in deep water (1000 to 4000 m) reflect the control of long-term thermohaline adjustment, which requires a much longer integration time to reach a quasi-steady state.

Fig. 3a shows the time series of the global annual mean SST for the last cycle in the OMIP1 (red) and OMIP2 (blue) experiments. Both time series show similar variations from the observations (black), capturing a few El Niño/La Niña events (e.g., 1968, 1983, 1997, 1998, 2016). At the same time, a slowly increasing trend in the mean SST can be found in both experiments, which is consistent with the observations.

As a result of the temperature increase, a decline in Arctic sea-ice coverage (SIC) is also evident in both experiments and the observations (Fig. 3b), while Antarctic sea-ice coverage shows a relatively steady state until 2014 (Fig. 3c). Note that in both the Arctic and Antarctic, our simulated results slightly underestimated the SIC compared to the observational mean, but the interannual variability looks similar

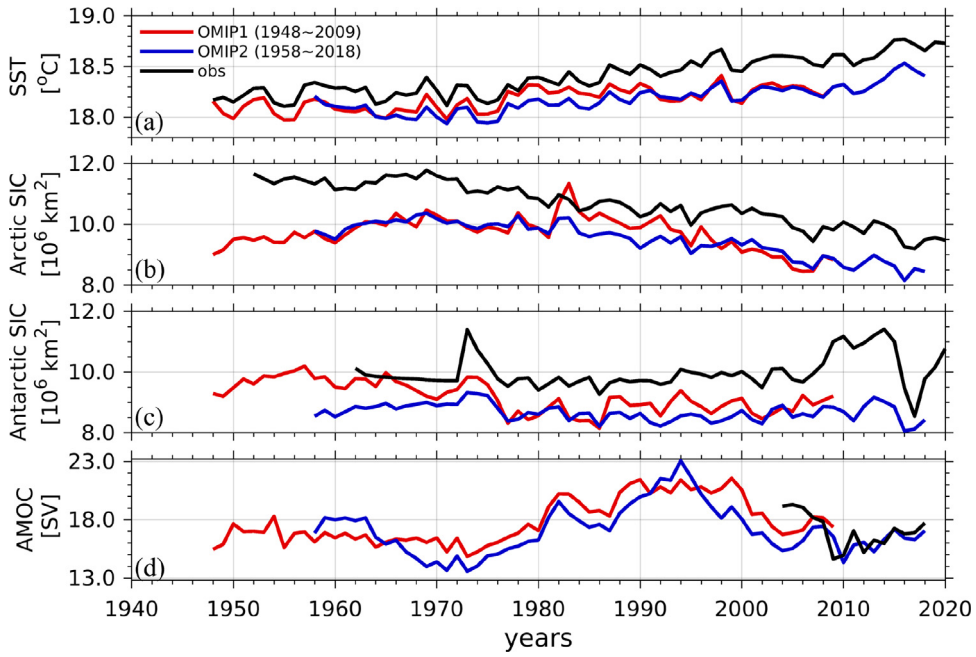

Fig. 3. Time series of global annual mean (a) SST, (b) Arctic SIC, (c) Antarctic SIC, and (d) AMOC transport at 26.5 °N for the last cycle in the OMIP1 (red) and OMIP2 (blue) experiments. The observations (black) from HadISST and RAPID are superimposed for comparison.

(significant at a 99% confidence level). Particularly, the time series correlation between the Arctic SIC in OMIP2 and the observations is higher than 0.9. This similarity suggests that the interannual variability of Arctic and Antarctic SIC is mostly controlled by the surface forcing. Overall, both the OMIP-1 and OMIP-2 experiments capture most of the observed temporal features.

We also use the AMOC at 26.5 °N as an interannual indicator of the AMOC strength. Fig. 3d compares the simulated AMOC transport in both the OMIP1 and OMIP2 experiments. Particularly, the AMOC transport time series in OMIP2 agrees reasonably well with the observations since 2004, which is when observational data is available. We successfully reproduce the increasing AMOC trend observed in recent years, as shown by the RAPID observations. However, Tsujino et al. (2020) found that all of the participating models except FSU-HYCOM showed a declining AMOC trend in recent years, raising discussions and concerns about possible issues with OMIP2 forcing in the North Atlantic. Fig. 4 suggests that the increased AMOC after 2010 is a robust feature within our OMIP2 experiments regardless of cycles. The uniqueness of this result compared to the majority of the other models may possibly provide helpful information concerning the multi-model diversity addressed in Tsujino et al. (2020) (further discussed in Section 4).

3.2. Spatial patterns

Fig. 5 compares the spatial patterns of the SST biases with the WOA13 climatology (Boyer et al., 2014). The last 30 years (1980–2009) of OMIP1 are used for a fair comparison. Both the OMIP1 and OMIP2 experiments can reasonably reproduce the general observational pattern. The global root-mean-square error (RMSE) biases of the SST are 0.79 °C and 0.71 °C in OMIP1 and OMIP2, respectively. Common SST biases across the OMIP1 and OMIP2 experiments show patterns similar to those suggested in many climate models (Dong et al., 2021; Golaz et al., 2019; Held et al., 2019); there tend to be cold biases in the Arctic Ocean, and there are generally warmer biases in the Southern Ocean. Warmer biases are located in many coastal upwelling regions, while slightly colder biases are found in the subtropical open ocean. Large biases in the western boundary currents, the Antarctic Circumpolar Current and Agulhas Current, are common in global models (Tsujino et al., 2020), likely due to the limitations of the horizontal resolution. Chassignet et al. (2020) showed improvements in these eddy-rich regions in higher-resolution ocean models. By comparison, our RMSE is reduced from 0.79 in OMIP1 to 0.71 in OMIP2, similar to the results of Tsujino et al. (2020), who found that OMIP2 shows reduced warm biases near the eastern boundary region of the Pacific Ocean. These conclusions also apply when the PHC2 climatology is used for comparison (Fig. 6).

As for the SSS, the RMSE of the biases is 0.43 in both experiments. There is a mixture of slightly fresher and saltier biases located at high latitudes, while some saltier biases are found in the tropical regions near the coast. These large-scale bias patterns are generally similar, except in the Arctic, regardless of the observational data used (Fig. 6). However, all simulated salinities are closer to PHC2 than WOA13, as expected, given that our model is weakly restored to the PHC2 data. Better RMSEs (0.31/0.30 for OMIP1/OMIP2) can be found for the PHC2 climatology, particularly in the high latitudes and certain coastal regions with large river runoffs. We note that the salinity fields of WOA13 and PHC2 differ significantly in the Arctic and many coastal regions (e.g., contours in Figs. 1 and 2 of Tseng et al., 2016a). The lowest salinity in PHC2, at the Amazon River mouth, is below 20 psu, while the lowest salinity in WOA13 is above 32 psu, see Table 2 in Tseng et al. (2016a). More coastal grid points are excluded in WOA13 than in PHC2, possibly due to its quality control procedures. PHC2 is also much saltier in the Arctic, as shown in Fig. 7 of Tsujino et al. (2020). The differences between different climatologies are beyond the scope of this study but must be considered in model comparison and validation procedures.

Furthermore, our results show a spatial difference between OMIP2 and OMIP1 similar to that described in Lin et al. (2020) and Tsujino et al. (2020), with OMIP2 having higher and lower salinities in the southern and northern hemispheres, respectively. OMIP2 also has a lower salinity in the Arctic near Greenland, which reduces the salty bias in OMIP1. In the Antarctic, the lower salinity in OMIP2 exacerbates its bias. We note that our OMIP1 and OMIP2 experiments are both restored to PHC2 (Steele et al., 2001), so the differences between them are not as obvious as those mentioned in Tsujino et al. (2020), where some OMIP2 experiments are restored to WOA13.

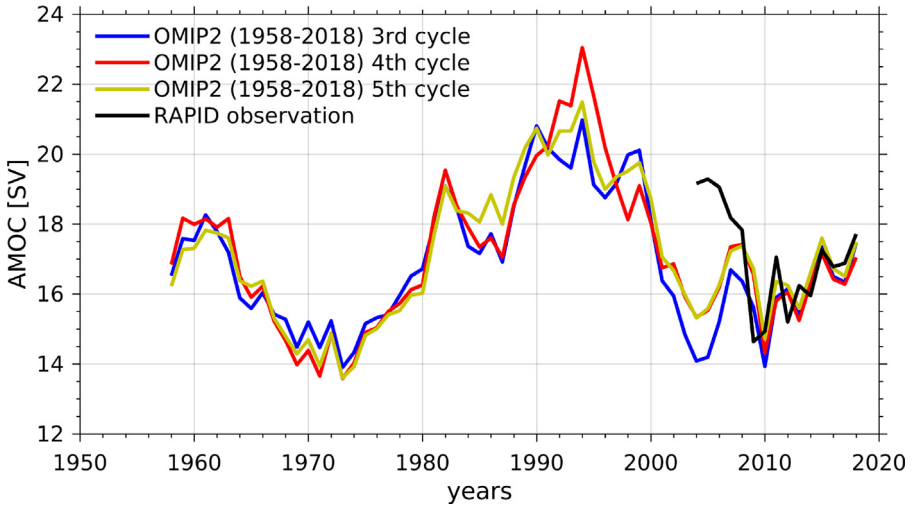

Fig. 4. AMOC transport at 26.5 °N in the 3rd, 4th, and 5th cycles of the OMIP2 simulation (units: Sv).

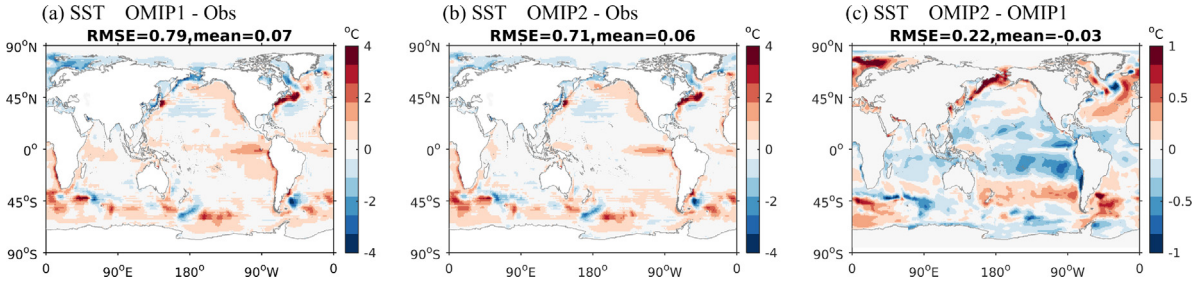

Fig. 5. Spatial pattern of (a) OMIP1 SST biases (°C), (b) OMIP2 SST biases (°C), in terms of the deviation from the WOA13 climatology. The last 30 years (1980–2009) of OMIP1 are used for a fair comparison. (c) The difference between OMIP1 and OMIP2 SST biases.

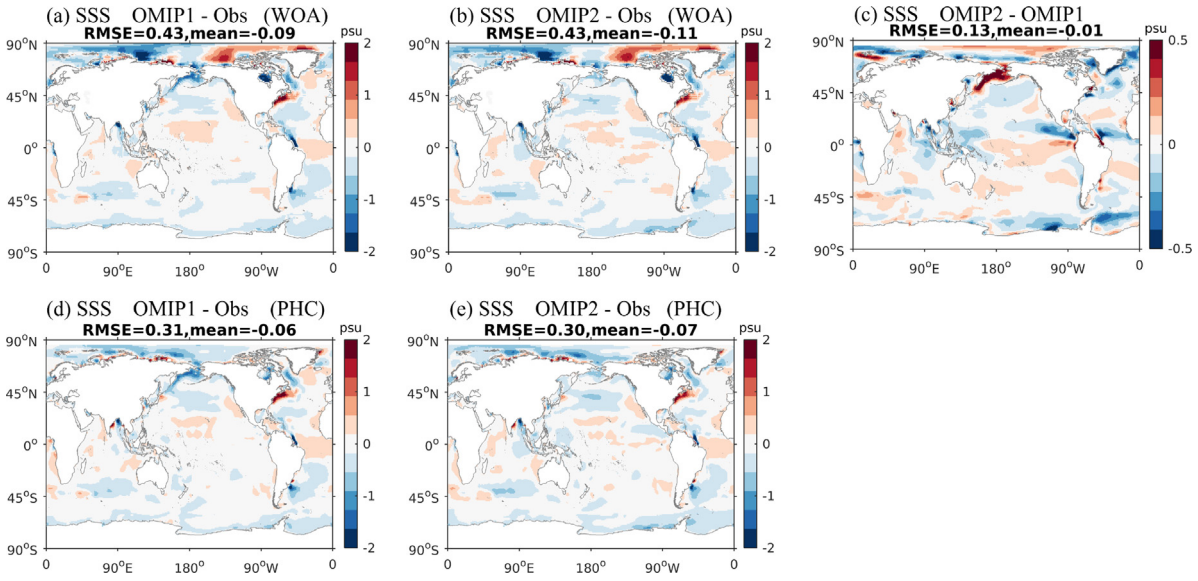

Fig. 6. Spatial pattern of (a) OMIP1 SSS biases (psu), (b) OMIP2 SSS biases (psu), in terms of the deviation from the WOA13 climatology. The last 30 years (1980–2009) of OMIP1 are used for a fair comparison. (c) The difference between OMIP2 and OMIP1 SSS biases. (d) OMIP1 SSS biases (psu), and (e) OMIP2 SSS biases (psu) but the model outputs are compared to the PHC2 climatology.

The observed and simulated mean mixed layer depths (MLDs), which determine the ocean interior ventilation, are compared in Fig. 7. We show that the model successfully captures the main spatial features of deep MLDs in the Northern Atlantic and Southern Ocean shown by the observations (the spatial pattern correlations with the observations are 0.58 and 0.53 for OMIP1 and OMIP2, respectively). However, we can see slightly deeper MLD biases in the subtropical oceans and shallower MLD biases primarily in the subarctic Pacific. Additionally, the very deep MLDs located in the Weddell Sea are not found in the observations. These findings are similar to some of the model results

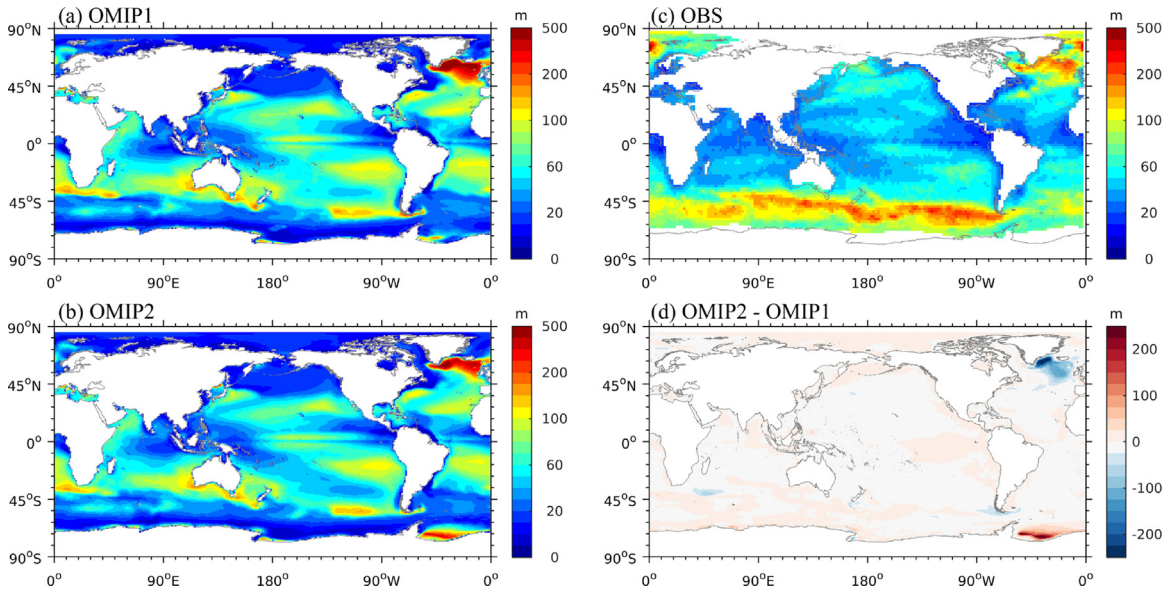

Fig. 7. Spatial pattern of the annual mean (a) OMIP1 MLDs (m) and (b) OMIP2 MLDs (m). (c) Observed MLD from dataset compiled by de Boyer Montégut et al. (2004). (d) The difference between OMIP2 and OMIP1 MLDs. Here, the MLD is defined as the deepest grid within 0.03 kg m^{-3} of density change from the topmost grid criteria. The last 30 years (1980–2009) of OMIP1 are used for the comparison.

in Tsujino et al. (2020), which suggest a large model spread in the regions of deep water formation. Compared with OMIP1, OMIP2 generally produces similar MLD results, but it shows shallower MLDs near Greenland. This may be caused by the larger freshwater discharge in the JRA55-do data. The other deeper MLDs in OMIP2 near the Weddell Sea region are possibly due to unreasonable deep water formation.

The observed and simulated mean sea-surface heights (SSHs), which represent the dynamical properties of the ocean, are compared in Fig. 8. The model can reasonably capture the key features of observational SSHs, with significant pattern correlation coefficients of 0.98 and 0.97 for OMIP1 and OMIP2, respectively. This indicates a reasonable simulation of upper ocean circulation. Higher SSHs are commonly located near the western boundaries in both the Atlantic and Pacific, while lower SSHs are found mainly in the eastern regions, as expected. OMIP2 shows higher SSHs in most of the Pacific region but lower SSHs in the western Pacific in the regime of the North and South equatorial current compared to OMIP1 (Fig. 8d). As discussed in Tsujino et al. (2020) and Hsu et al. (2021), this may be likely due to the decreased wind stress in OMIP2 and significant wind stress curl differences near the Intertropical Convergence Zone (ITCZ). Sun et al. (2021) also suggested the weakened wind stress in the OMIP2 forcing thus results in weaker westward North and South Equatorial Currents. These results suggest that the differences shown here may not be easily explained by the wind stress strength. We also find distinct SSH differences between OMIP2 and OMIP1 along the Antarctic Circumpolar Current; these differences are presumably related to the weaker winds in OMIP2. Higher SSHs near the Arctic in OMIP2 may be connected with the lower upper-ocean salinity (discussed later), which produces less dense water.

The barotropic stream function, defined as the depth-integrated ocean volume transport, provides important information about the mean current and gyre circulation. Fig. 9 shows the simulated barotropic stream function, reflecting the position of the equatorial current, basin subtropical gyres, and a distinct strong eastward transport in the Antarctic Circumpolar Current. The spatial patterns are similar to those found in observations (Colin de Verdière and Ollitrault, 2016) and other models (Sidorenko et al., 2015; Stammer et al., 2018). Compared with OMIP1, OMIP2 shows a weaker eastward transport along Kuroshio Extension and Gulf Stream and most notably the Antarctic Circumpolar Current, which are shown in blue (Fig. 9). These differences are highly consistent with the SSH difference caused by the weaker winds in OMIP2 (Fig. 8).

The transport in the Antarctic Circumpolar Current can be quantitatively assessed through the Drake Passage transport (Fig. 10), as the Drake Passage is the major passage in the Southern Ocean. Both the OMIP1 and OMIP2 Drake Passage transports are within or close to the range of observational estimates (Donohue et al., 2016) with a slightly higher bias; they show an increasing trend in the Antarctic Circumpolar Current after 1980, possibly related to ocean warming (Shi et al., 2021). However, our estimated transports (ranging from 165 to 200 Sv) belong to the higher transport group compared to other model studies (Tsujino et al., 2020). This could be related to the higher density of the simulated Antarctic Bottom Water along with a strong abyssal overturning circulation cell (over 16 Sv) in the Global Meridional Overturning Circulation (GMOC), which will be further discussed later.

Finally, the sea-ice distribution is also very important for the ocean–sea ice coupled simulations (Fig. 11). In the Northern Hemisphere, the sea-ice extent in OMIP2 is very close to the observations in March, but it is slightly underestimated by the model in September (Fig. 11a). In the Southern Hemisphere, the simulation results show a smaller sea-ice extent compared to observations in both March and September. Our SIC differences between OMIP2 and OMIP1 are consistent with those shown in Tsujino et al. (2020). In the Northern Hemisphere, both OMIP1 and OMIP2 reproduce similar SICs during March, while the Arctic SIC in OMIP1 is further underestimated during September (Fig. 11b). In the Southern Hemisphere, OMIP2 also has a larger sea-ice extent than OMIP1 in March; OMIP2 provides a sea-ice extent that is closer to the observations. However, OMIP2 generates a smaller sea-ice extent than OMIP1 in September, and due to the common smaller sea-ice extent bias in our model, OMIP2 deviates slightly more from the observations, as shown previously in Fig. 3.

3.3. Zonal means

We further evaluate the zonal mean ocean temperature and salinity biases of OMIP2 across each basin over the last 30 years of the OMIP1 experiment in Fig. 12a, b. We divide the global ocean into three basins: the Southern Ocean (86 °S–35 °S); the Indian Pacific Ocean (35 °S–65 °N); and the Arctic and Atlantic oceans (35 °S–90 °N). Both temperature and salinity biases show similar patterns due to the compensating effect of density. In the Southern Ocean, the zonal mean temperature bias exhibits a quasi-cold (south) / warm (north) pattern,

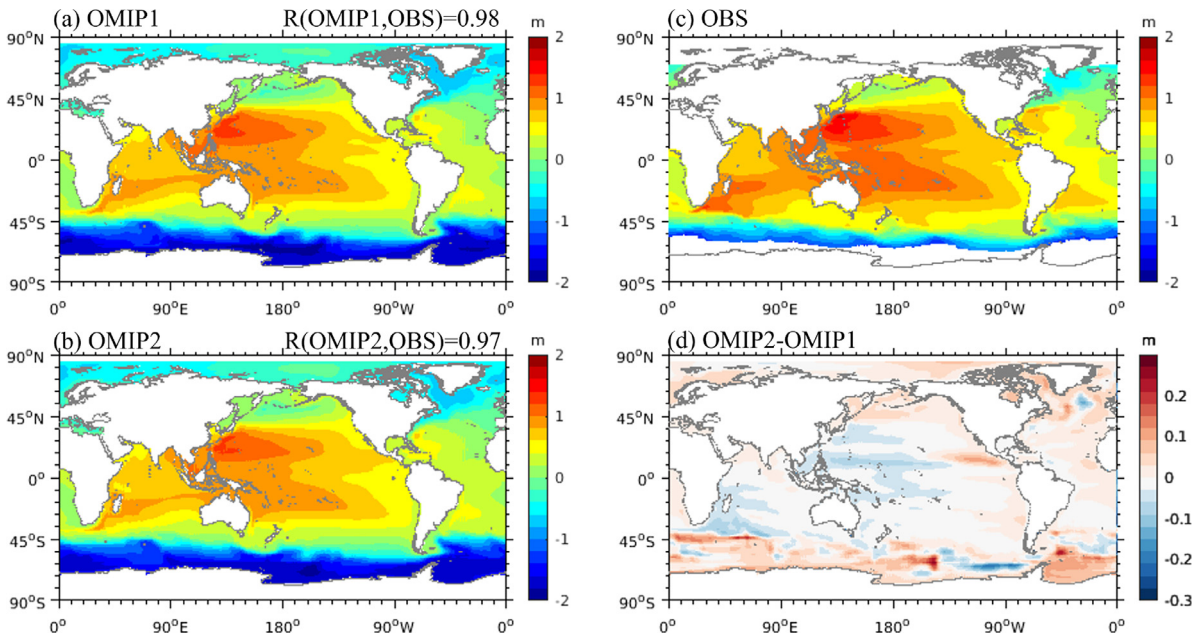

Fig. 8. This figure is the same as Fig. 7 except that it describes the SSH (m). The last 17 years (1993–2009) of OMIP1 are compared with the available AVISO observations.

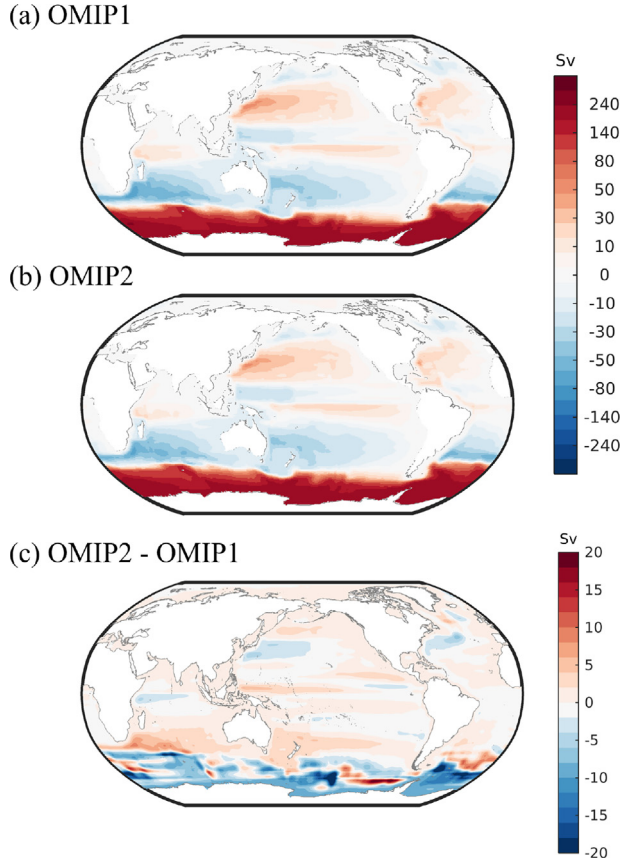

Fig. 9. Spatial pattern of simulated barotropic stream function (units: Sv) in the (a) OMIP1 and (b) OMIP2 experiments, and (c) the difference between OMIP2 and OMIP1. The last 30 years (1980–2009) of OMIP1 are used in the comparison.

similar to the ensemble bias shown in Tsujino et al. (2020). In the Indian-Pacific Basin, a similar pattern can be found: there is a warm and salty bias in the upper ocean (from the surface to depths of 400 m in the tropics and down to 1 km in the high latitudes), and a slightly cold and fresh bias is located deeper in the ocean interior. The Arctic and Atlantic oceans also show overall warm and salty biases in the upper ocean, from the surface to approximately 3 km depth (most significantly around 60 °N, which is near the region of deep water formation). Cold and fresh biases are shown around 30 °N at 1 km depth and in the deep to bottom ocean in the North Atlantic. This may be related to the insufficient Mediterranean overflow water migrating downward to the observed equilibrium depth in the North Atlantic (Dietrich et al., 2008). Since no specific overflow parameterization (e.g., Danabasoglu et al., 2012) is imposed here, except an artificial broadening of the narrow Strait of Gibraltar (it is roughly 3 times wider in the simulation than it is in reality), the representation of the density overflow current is still unrealistic in terms of the downward propagation. The broadening attempts to ensure a reasonable Mediterranean outflow transport (~1 Sv), but the relatively coarse resolution (both horizontally and vertically) still cannot fully resolve the downward penetration of the density overflow current (Tseng and Dietrich, 2006), leading to the saline (fresh) biases above (below) 0.8 km. Some of these patterns are very similar to the biases shown in Tsujino et al. (2020), suggesting that there are common biases due to the OMIP2 forcing and the lack of proper parameterization.

Compared with OMIP1, OMIP2 produces colder and fresher water in the higher latitudes and warmer and saltier water in the lower latitudes of the Southern Ocean. In the Indian-Pacific, OMIP2 in particular reduces the warm bias shown in OMIP1; it shows distinctively colder temperatures in the upper ocean near the equator (Fig. 12c). Both of these differences between OMIP2 and OMIP1 are similar to the findings of Tsujino et al. (2020). A particular feature of TIMCOM is the following notable difference. In the Atlantic, OMIP2 has colder and fresher water than OMIP1 around 40–50 °N, but it also has warmer and saltier water in the Arctic region. Both differences extend to the deep ocean (~4 km) and thus they may be related to slight differences in the location for Atlantic Deep Water Formation, which likely leads to the weaker meridional ocean circulation in OMIP2 (Fig. 13c).

The zonal-averaged salinity and its distribution across each basin are also controlled by the meridional ocean circulation. Fig. 13a, b shows the AMOC and GMOC. Both OMIP1 and OMIP2 can reasonably reproduce the strong Atlantic northward transport around 35–40 °N from the surface to a depth of 1 km, the North Atlantic Deep Water between depths of 1 km and 2.5 km, and Antarctic Bottom Water at depths below 2.5 km. The maximum AMOC transport at 26.5 °N from

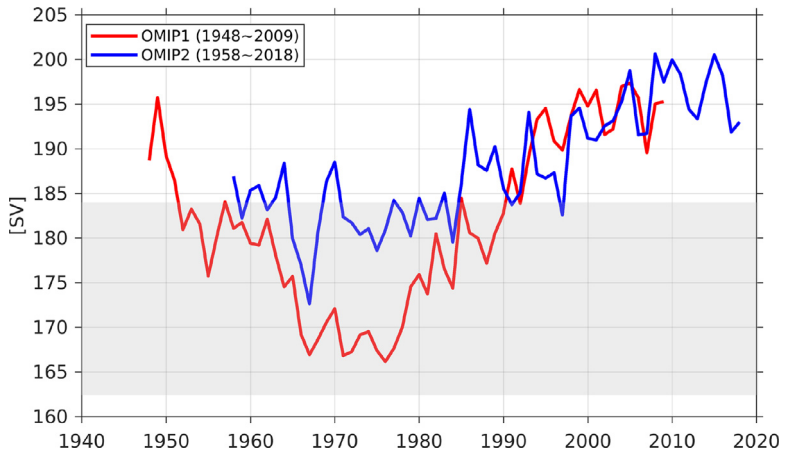

Fig. 10. Simulated Drake Passage transport (units: Sv, positive eastward) in OMIP1 (red) and OMIP2 (blue); the Drake Passage transport represents the strength of the Antarctic Circumpolar Current. The observational estimate is 173.3 ± 10.7 Sv; it is based on Donohue et al. (2016).

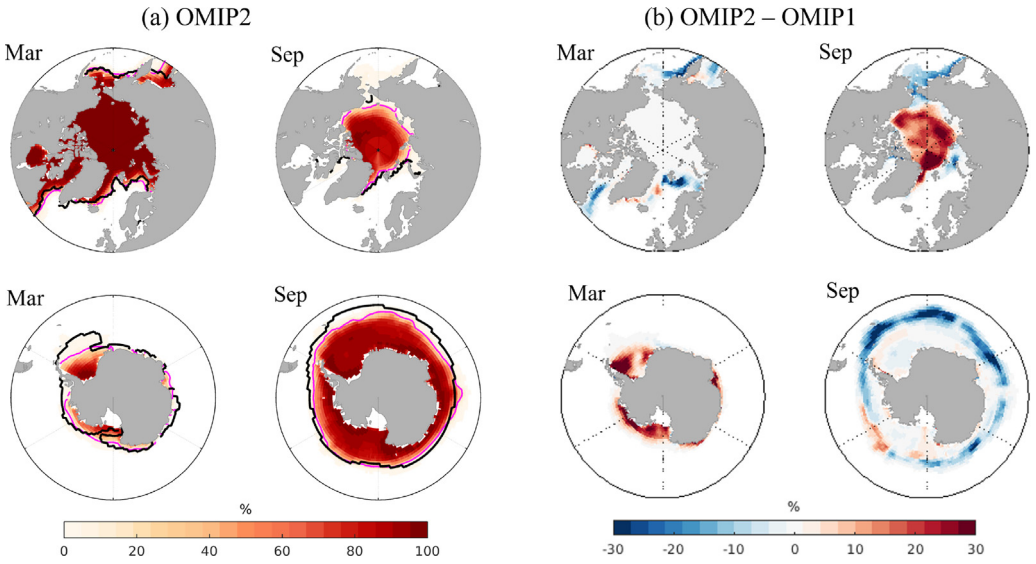

Fig. 11. (a) Spatial pattern of March and September SIC (%) in OMIP2 over the last 30 years (1980–2009) of the OMIP1 experiment. Pink lines are contours of 15% ice concentration (observations are superimposed as black contours). (b) Differences between the OMIP2 and OMIP1 experiments.

2005–2009 in OMIP1 and OMIP2 is slightly less than the transport according to the RAPID observations (Fig. 13e) when they are integrated down to around 1 km depth (17–18 Sv). Moreover, as shown earlier in Fig. 4, our OMIP2 successfully reproduces the increase of the AMOC seen in the observations after 2010; thus, from 2010–2018, the maximum AMOC closely matches the observational value. However, we note that our simulated AMOC is largely restricted to the upper 3 km, which is shallower than the RAPID observations and past literature estimates (McCarthy et al., 2015) of around 4 km. We also simulate a relatively strong deep to bottom cell (~16 Sv) in the deep water overturning circulation compared to other modeling results (Fig. 13b). Compared with OMIP1, OMIP2 shows a weaker overturning circulation, including a counterclockwise cell in the Atlantic (Fig. 13c), and the overturning circulation is also globally weaker in the Southern Ocean and Northern subtropical Cell (Fig. 13d). The weaker overturning circulation can relate to the weaker wind stress in OMIP2. Our result shows a slightly stronger counterclockwise deep to bottom cell at depths below 3 km in OMIP2, which is also similar with the findings of other model results in Tsujino et al. (2020), suggesting a stronger deep water formation and possibly explaining the cooling in the bottom water in Fig. 2c.

Closely linked with the overturning circulation, the zonally averaged Atlantic and global heat transports for the period from 1958–2004 are assessed in Fig. 14. The Atlantic northward heat transport reaches its maximum between 20 and 30 °N, while the global heat transport shows a maximum northward transport around 20 °N and a maximum southward transport around 10 °S. Similar to other results in Tsujino et al. (2020), the northward transport is slightly lower than the transport according to the observations, but it is very close to the recently reported value of the peak heat transport in the North Atlantic of 1.0 ±0.1 PW. Compared with OMIP1, OMIP2 shows slightly lower heat transports for the Atlantic and globally, presumably caused by the weaker meridional overturning circulation (both in the AMOC and GMOC, as shown earlier) and also the lower wind speed in OMIP2 (Taboada et al., 2019).

4. Recent increase of AMOC starting in 2010

Although many studies have associated a decline in the AMOC with temperature warming since the 1980s and projected a possible decrease until the end of the century (Weijer et al., 2020), our model shows a recent recovery and increase of the AMOC starting in 2010 that is also present in observations (Moat et al., 2020). Nevertheless, this feature has not been captured in many other OMIP2 experiments (Tsujino et al., 2020); some studies express concerns that the bias may come from

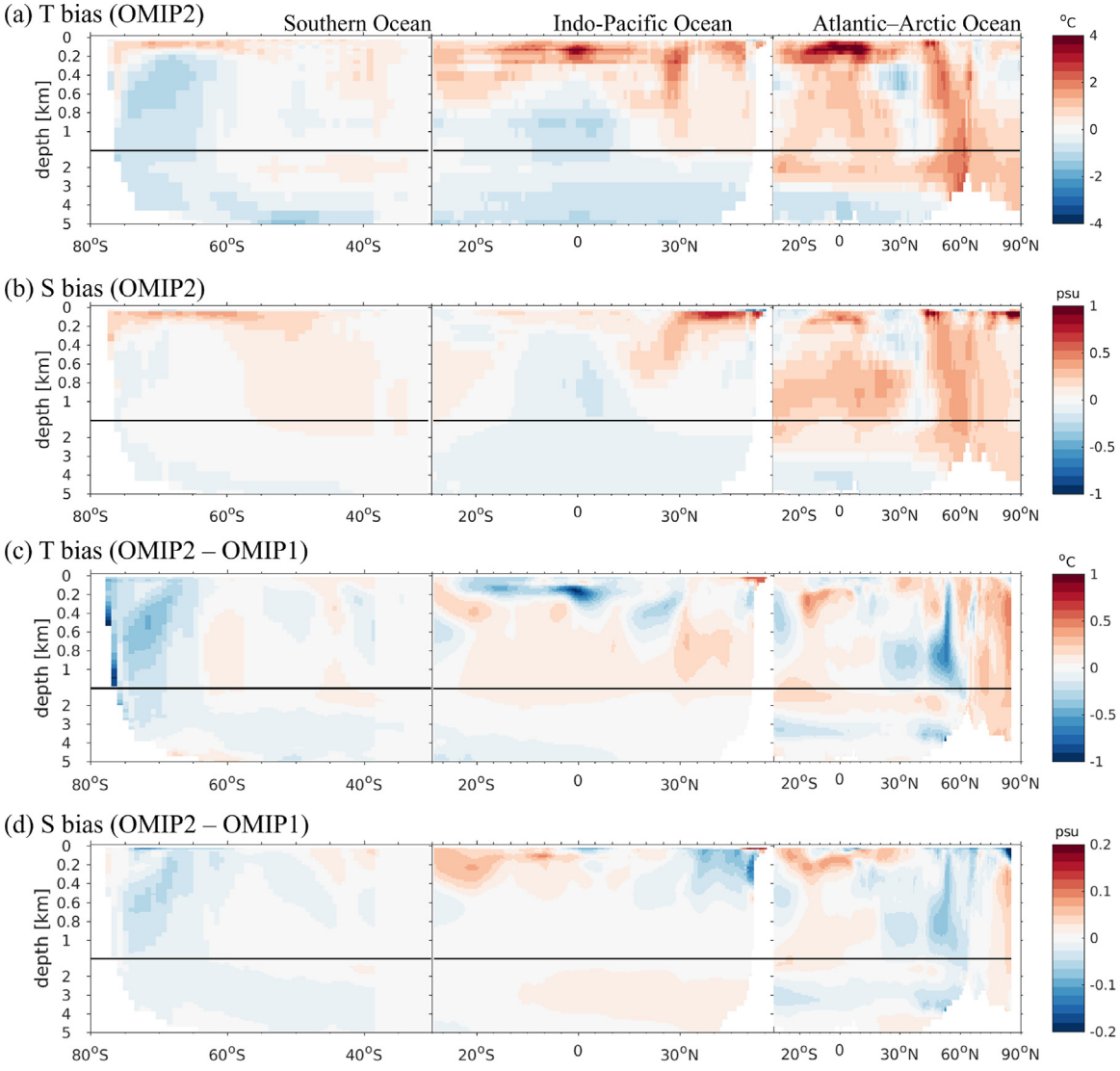

Fig. 12. Latitude–depth plot of the zonal mean (a) ocean temperature bias (°C) and (b) salinity bias (psu) in the Southern Ocean, Indo-Pacific Ocean, and Atlantic–Arctic Ocean basins for OMIP2 over the last 30 years of the OMIP1 experiment. Observations are from WOA13v2.

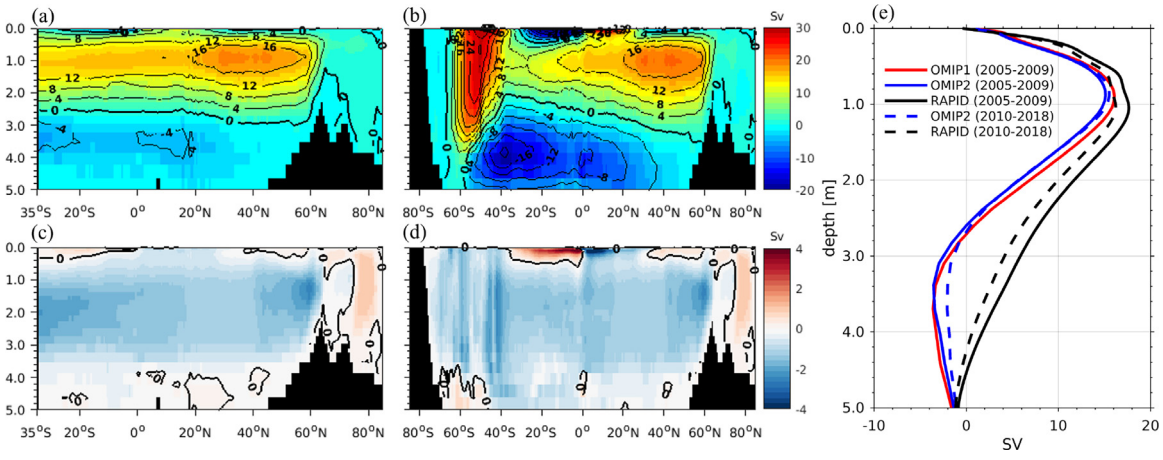

Fig. 13. Simulated mean (a) AMOC and (b) GMOC over the last thirty years (1980–2009) of the OMIP1 experiment (units: Sv). (c, d) Differences in AMOC and GMOC between OMIP2 and the corresponding OMIP1 experiments (a, b). (e) Vertical profiles of the time-averaged circulation at 26.5 °N (2005–2009) for OMIP1 (red), OMIP2 (blue), and observations from RAPID (black), as well as for averaged OMIP2 data (blue dashed line) and RAPID observations (black dashed line) (2010–2018).

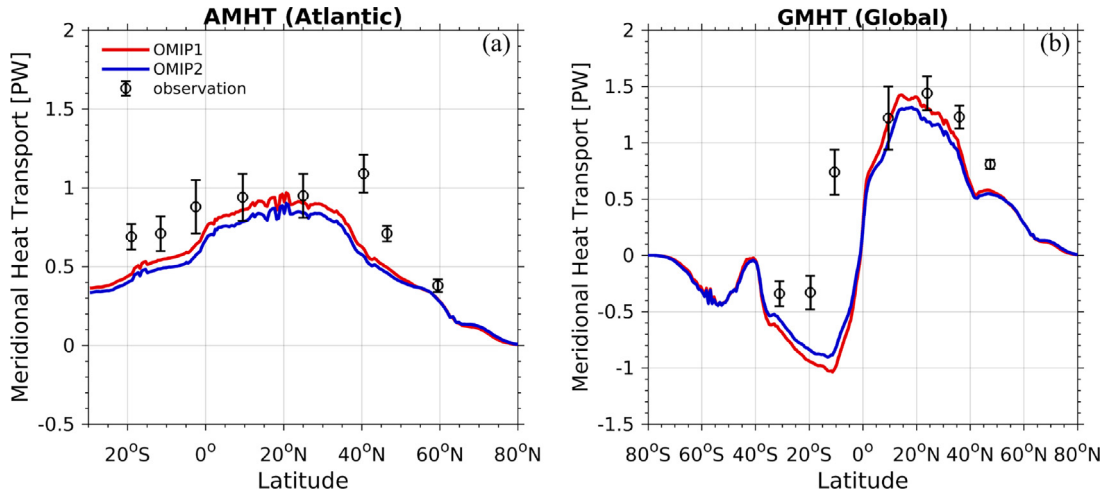

Fig. 14. Simulated mean (a) Atlantic northward heat transport and (b) global northward heat transport from 1958–2004 (units: PW = 10^{15} W m^{-2}) for OMIP1 (red) and OMIP2 (blue), respectively. Observations (black) (Zheng and Giese, 2009) averaged within the same time range are superimposed.

the JRA55-do dataset (Tsujino et al., 2018). We thus further explore potential mechanisms in our model that drive the recent increase of the AMOC that seen in the observations.

The AMOC variability is directly controlled by the density anomalies in the North Atlantic where deep water forms (Danabasoglu et al., 2012), and the recent increase of the AMOC has been shown to follow a rise in the density flux driven by fast cooling, enhancing the water mass transformation (Desbruyères et al., 2019). We estimate the surface density flux in our simulation based on Marsh (2000) using Eq. (1) below; it combines the net effects of the heat flux and freshwater change on the density (Schmitt et al., 1989).

$$D = \frac{\alpha(T,S)}{C_p} Q + \rho_0 \beta(T,S) \frac{S}{(1-S)} (E-P). \quad (1)$$

The first term represents the density changes due to the net heat flux (Q, positive is upward, units: W m^{-2}), and α is the thermal expansion coefficient. The second term represents the changes due to evaporation and precipitation ($E - P$, units: kg m^{-2} s^{-1}), and β is the haline contraction coefficient (Marsh, 2000) calculated from T (°C) and S (psu) according to the equation of state (Friedrich and Levitus, 1972). C_p is the specific heat of seawater (4000 J kg^{-1} K^{-1}), and ρ_0 is the reference density for seawater (1025 kg m^{-3}).

Fig. 15 further shows that the time series of the surface density flux over the North Atlantic (45–65 °N) in our simulation resembles the modeled AMOC variability over the last few decades. Particularly, we can find a similar recovery and increasing trend in the twenty-first century. The peak of the surface density flux in the 1990s seems to lead (or roughly match) the peak of the AMOC a few years earlier. Our results confirm the findings of Desbruyères et al. (2019), who showed that the surface density change may be a leading and driving predictor of AMOC variability. The variability of the surface density flux is mainly driven thermally by changes in the surface heat flux (represented by the green line in Fig. 15). Thus, we conclude that the recent increase of the AMOC is likely controlled by surface cooling in the high latitudes of the North Atlantic that is possibly associated with the extreme low-air-temperature events over the North Atlantic caused by atmospheric variability (Josey et al., 2018). As surface water cools faster, density fluxes increase and then sink, potentially strengthening the AMOC.

We also found that the vertical mixing coefficient for salinity (VDC), particularly the top 0–30 m for the latitude higher than 45 °N, may be a critical key to successfully simulate the recent thermally driven AMOC increase. A sensitivity experiment with a 10 times larger VDC for the top 0–30 m salinity significantly reduces the increasing trend (Fig. 16). Both experiments (low VDC and high VDC) are initialized from the same initial condition at the end of 2013 and run for 5 years (2014–2018). The low VDC simulation shows an increase of AMOC, while the high VDC simulation shows a non-trivial trend of AMOC, resembling to the common results from the OMIP2 ocean model comparison (Tsujino et al., 2020).

As shown in Fig. 16b, the smaller turbulent eddy diffusivity in the salinity (low VDC) lowers the vertical mixing of arctic freshwater near the surface, leading to a salinity maximum around 40 m depth (red dashed line on Fig. 16d) which may separate the subsurface water from the surface. The temperature profiles are compensated accordingly owing to the salinity changes (Fig. 16c, d). Thus, in the low VDC simulation, the density near the level of salinity maximum is higher with lower density can be found above (red solid line on Fig. 16e). As a result, stronger stratification are formed between surface and subsurface layers (Fig. 16e). The stronger stratification in the upper ocean can react with more sensitivity to temperature variability in the atmosphere by keeping the anomaly signals within the stratified upper ocean, and thus allowing the cold event in the recent five years to create the stronger density flux, reproducing the observational AMOC increase.

Our analysis provides mechanistic insights to community and also presents a possible model design reference for other ocean models to follow in addressing the recent AMOC bias in OMIP2 experiments next. Here, we find the near surface vertical mixing for salinity in the Arctic and north of 45°N in the North Atlantic seems to effectively determine the AMOC intensity at some critical levels while the AMOC strength is not so sensitive to the change of VDC in the temperature and deeper ocean. Further study is required in the future to investigate the fundamental mechanism, which may relate to the sea ice distribution and MLD biases north of 45°N. We also want to note that all models have different levels of surface restoring, which may complicate the vertical mixing adjustment related to the recent AMOC change.

5. Discussion and summary

This study presents the design and a detailed description of TIM-COM for CMIP6 participation, as well as the evaluation of the model's performance in the OMIP1/OMIP2 experiments. The general features compare well with observations temporally and spatially. Some model biases are similar to those described for many other models in Tsujino et al. (2020), including the temperature and salinity biases in the eddy-rich western boundary currents and Southern Ocean, and the deep MLD bias in the Weddell Sea. Particularly, many differences across spatial and zonal average fields between OMIP2 and OMIP1 can be primarily attributed to the weaker tropical/subtropical winds and fresher salinity in the Arctic caused by the OMIP2 forcing.

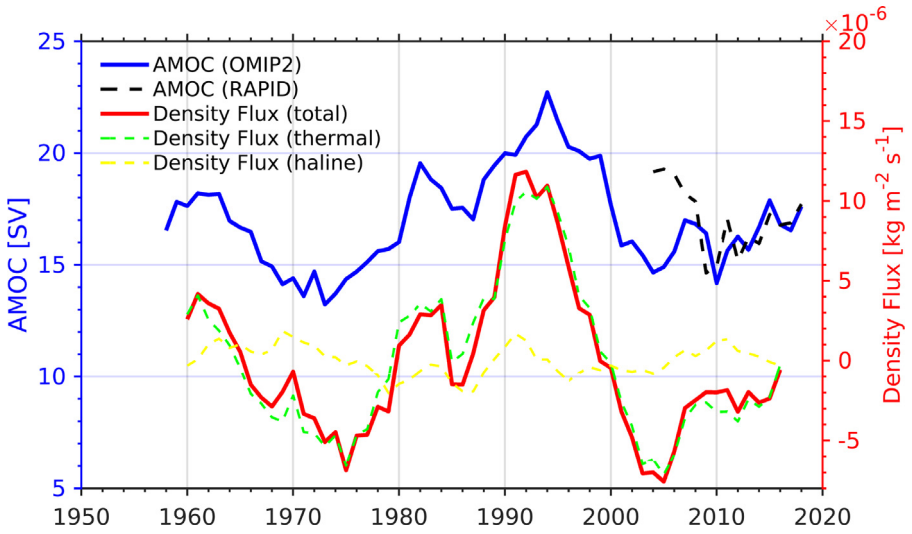

Fig. 15. (a) AMOC transport at 26.5 °N in the last cycle of the OMIP2 experiment (blue) and RAPID observations (black) (units: Sv). The 5 year running mean of the annual mean density flux over the North Atlantic (45–65 °N) is superimposed (red). The total density flux is separated into thermal (green) and haline (yellow) components.

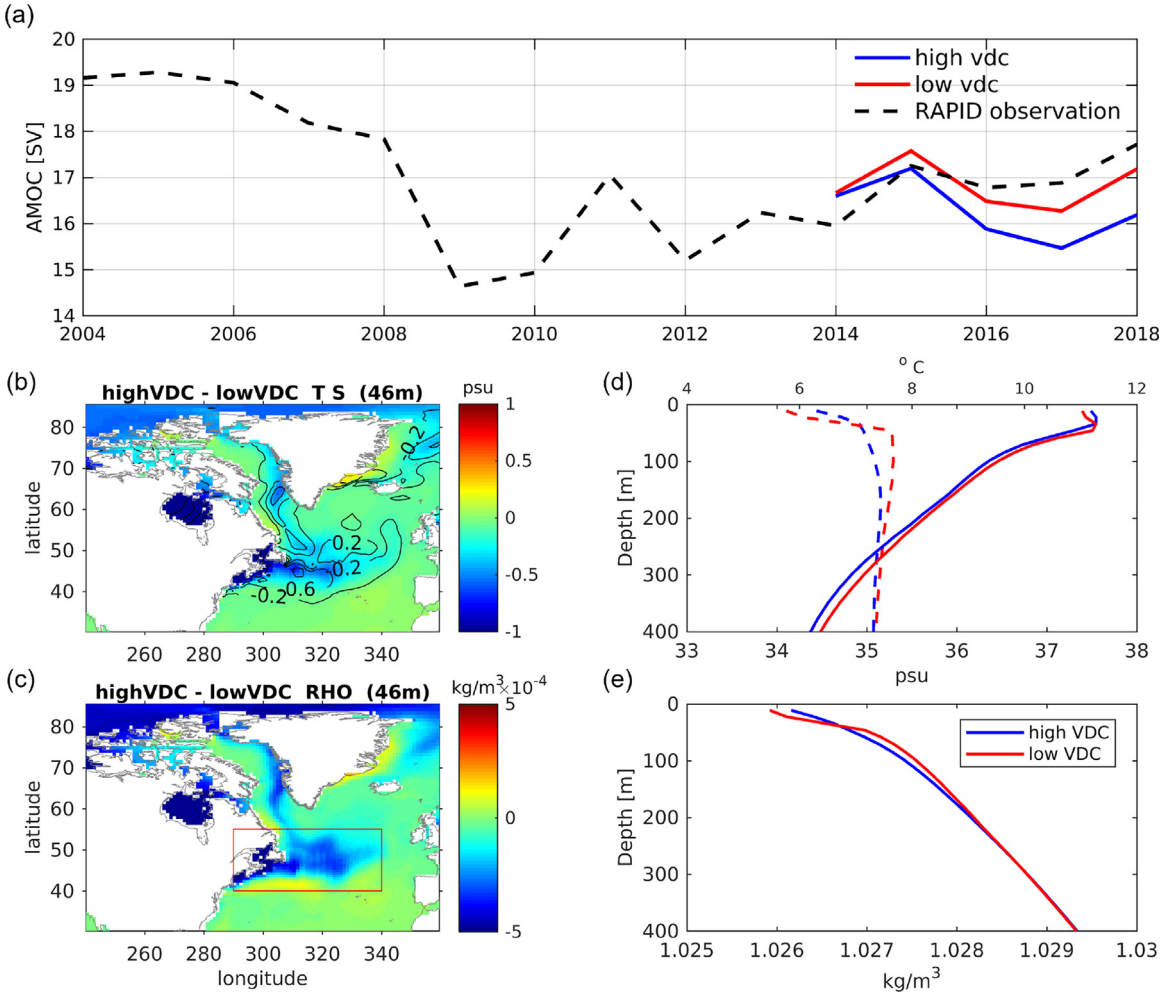

Fig. 16. (a) Comparison of AMOC transport at 26.5 °N between high (blue) and low eddy viscosity (red) of salinity at the surface ocean in the last five years of OMIP2 experiment and RAPID observations (black) (units: Sv). (b) The 5 year mean difference of temperature (shading), salinity (contour), and (c) density between high vdc and low vdc cases. The temperature, salinity, and density profile of the North Atlantic region highlighted by the red box is shown in (d) and (e).

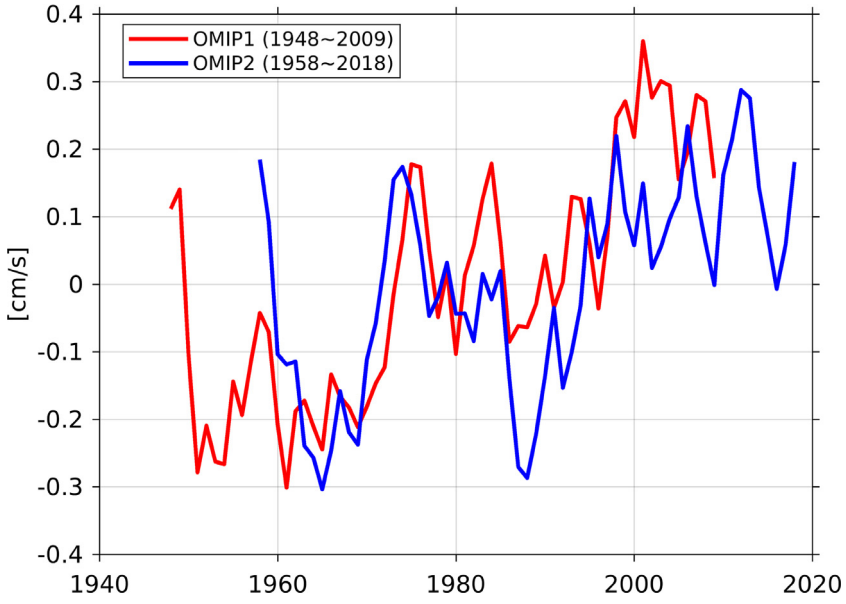

Fig. 17. Time series of upper 100 m zonal velocity (minus 2000 m velocity) averaged from 48–58°S for OMIP1 and OMIP2.

The Drake Passage transport seems to be high in this model compared to many other model studies. However, the overall Antarctic Circumpolar Current shows an increasing trend similar to the observations and many other studies (e.g., Shi et al., 2021). Fig. 17 shows the time series of the zonal mean velocity (it resembles Fig. 3a in Shi et al., 2021), which suggests that ocean warming is likely to continue to accelerate the Southern Ocean zonal flow.

Nevertheless, other existing biases still require further attention. (1) The polar sea-ice extent in our model is less than that of the observations. (2) The warmer zonal average bias in the Atlantic–Arctic Ocean AMOC circulation cell is shallower than the observations indicate, resulting in a stronger deep to bottom meridional cell. These biases could likely be interlinked with the higher Drake Passage transport through different mechanisms, such as the negative feedbacks between the sea-ice extent and Antarctic Circumpolar Current (van Westen and Dijkstra, 2021), and also the links between a strong Antarctic Circumpolar Current and the bottom meridional cell, as discussed earlier. The uncertainty of the freshwater input in the Arctic/Antarctic may also be another possible factor (Tseng et al., 2016a). Further studies are required to investigate the possible linkages and sources of these model biases.

6. Data usage

Our simulation data from both OMIP1 and OMIP2 have been uploaded onto the Earth System Grid Federation (ESGF) data server and are available for download (https://esgf-node.llnl.gov/projects/cmip6/). The dataset format is NetCDF, version 4. The newer version used in this study, TaiESM1-TIMCOM2 (https://doi.org/10.22033/ESGF/CMIP6.16323), is shown along with the previous version, TaiESM1-TIMCOM (https://doi.org/10.22033/ESGF/CMIP6.14336). The newer version has the following differences: an increased number of vertical layers, adjusted GM parameters, and a slightly modified land mask area. The horizontal grid numbers of the model outputs are 320 and 288 in the zonal and meridional directions, respectively. The format is slightly changed to the CMOR (Climate Model Output Rewriter) file structure, as required by the OMIP. The data consist of 55 vertical levels, and the original vertical level is not changed on ESG nodes. The depths of the W grid and *T* grid are documented in

Table 1
Vertical depths of *T* and W grids. The temperature (T), salinity (S), pressure (P), and horizontal vectors (u, v) are located in the *T* grid, and the vertical velocity (W) is located in the W grid. The values represent the depth below Level 1 of the W grid (units: m).

Level	T-grid depth	W-grid depth
1	5.5	0.0
2	16.7	11.1
3	28.2	22.4
4	40.0	34.0
5	52.1	46.0
6	64.6	58.3
7	77.5	71.0
8	90.9	84.2
9	104.8	97.8
10	119.2	111.9
11	134.3	126.7
12	150.0	142.0
13	166.5	158.1
14	183.7	175.0
15	201.9	192.7
16	221.1	211.4
17	241.4	231.1
18	262.8	251.9
19	285.6	274.1
20	309.9	297.6
21	335.8	322.6
22	363.4	349.4
23	393.1	378.0
24	424.8	408.7
25	459.0	441.6
26	495.7	477.0
27	535.4	515.2
28	578.2	556.4
29	624.6	601.0
30	674.8	649.2
31	729.2	701.5
32	788.4	758.2
33	852.7	819.9
34	922.7	887.0
35	999.0	960.0
36	1082.2	1039.7
37	1173.0	1126.6

(*continued on next page*)

Table 1 (*continued*).

Level	T-grid depth	W-grid depth
38	1272.2	1221.5
39	1380.6	1325.2
40	1499.3	1438.6
41	1629.2	1562.7
42	1771.4	1698.6
43	1927.3	1847.5
44	2098.1	2010.7
45	2285.6	2189.7
46	2491.3	2386.0
47	2717.0	2601.5
48	2964.9	2838.1
49	3237.2	3097.9
50	3536.4	3383.3
51	3865.2	3697.0
52	4226.7	4041.7
53	4624.1	4420.7
54	5061.2	4837.5
55	5541.9	5295.8
56	–	5800.0

Table 1. The frequency of the data is monthly; the data cover a period of 1–372 years for OMIP1 and 1–362 years for OMIP2 (six cycles of the forcing data).

CRediT authorship contribution statement

Yu-Heng Tseng: Supervision, Methodology, Conceptualization, Writing – review & editing. **Shou-En Tsao:** Writing – original draft, Visualization. **Yi-Chun Kuo:** Investigation, Data curation. **Jia-Ying Tsai:** Software, Resources.

Declaration of competing interest

The authors declare that they have no known competing financial interests or personal relationships that could have appeared to influence the work reported in this paper.

Acknowledgments

Constructive comments from the anonymous reviewers are greatly appreciated. Computer time was made available by National Center for High-performance Computing (NCHC) of National Applied Research Laboratories (NARLabs) in Taiwan. Financial support by the National Science and Technology Council Grant 107-2611-M-002-013-MY4, 108-2111-M-002-006-MY3 and 111-2111-M-002-015, Taiwan, is appreciated.

References

Boyer, T.P., Garcia, H.E., Locarnini, R.A., Zweng, M.M., Mishonov, A.V., Reagan, J.R., Antonov, J.I., Baranova, O.K., Biddle, M.M., Johnson, D.R., et al., 2014. 2013 World Ocean Atlas aids high-resolution climate studies. EOS Trans. Am. Geophys. Union 95 (41), 369–370.

de Boyer Montégut, C., Madec, G., Fischer, A.S., Lazar, A., Iudicone, D., 2004. Mixed layer depth over the global ocean: An examination of profile data and a profile-based climatology. J. Geophys. Res. Oceans 109 (C12).

Chassignet, E.P., Yeager, S.G., Fox-Kemper, B., Bozec, A., Castruccio, F., Danabasoglu, G., Horvat, C., Kim, W.M., Koldunov, N., Li, Y., et al., 2020. Impact of horizontal resolution on global ocean–sea ice model simulations based on the experimental protocols of the ocean model intercomparison project phase 2 (OMIP-2). Geosci. Model Dev. 13 (9), 4595–4637.

Danabasoglu, G., Large, W.G., Tribbia, J.J., Gent, P.R., Briegleb, B.P., McWilliams, J.C., 2006. Diurnal coupling in the tropical oceans of CCSM3. J. Clim. 19 (11), 2347–2365.

Danabasoglu, G., Yeager, S.G., Bailey, D., Behrens, E., Bentsen, M., Bi, D., Biastoch, A., Böning, C., Bozec, A., Canuto, V.M., et al., 2014. North Atlantic simulations in coordinated ocean-ice reference experiments phase II (CORE-II). Part I: Mean states. Ocean Model. 73, 76–107.

Danabasoglu, G., Yeager, S.G., Kim, W.M., Behrens, E., Bentsen, M., Bi, D., Biastoch, A., Bleck, R., Böning, C., Bozec, A., et al., 2016. North Atlantic simulations in coordinated ocean-ice reference experiments phase II (CORE-II). Part II: Inter-annual to decadal variability. Ocean Model. 97, 65–90.

Danabasoglu, G., Yeager, S.G., Kwon, Y.-O., Tribbia, J.J., Phillips, A.S., Hurrell, J.W., 2012. Variability of the Atlantic meridional overturning circulation in CCSM4. J. Clim. 25 (15), 5153–5172.

Desbruyères, D.G., Mercier, H., Maze, G., Daniault, N., 2019. Surface predictor of overturning circulation and heat content change in the subpolar North Atlantic. Ocean Sci. 15 (3), 809–817.

Dietrich, D.E., Tseng, Y.-H., Medina, R., Piacsek, S.A., Liste, M., Olabarrieta, M., Bowman, M.J., Mehra, A., 2008. Mediterranean overflow water (MOW) simulation using a coupled multiple-grid Mediterranean Sea/North Atlantic Ocean model. J. Geophys. Res. Oceans 113 (C7).

Dong, X., Jin, J., Liu, H., Zhang, H., Zhang, M., Lin, P., Zeng, Q., Zhou, G., Yu, Y., Song, M., et al., 2021. CAS-ESM2. 0 model datasets for the CMIP6 ocean model intercomparison project phase 1 (OMIP1). Adv. Atmospheric Sci. 38 (2), 307–316.

Donohue, K., Tracey, K., Watts, D., Chidichimo, M.P., Chereskin, T., 2016. Mean antarctic circumpolar current transport measured in drake passage. Geophys. Res. Lett. 43 (22), 11–760.

Eyring, V., Bony, S., Meehl, G.A., Senior, C.A., Stevens, B., Stouffer, R.J., Taylor, K.E., 2016. Overview of the coupled model intercomparison project phase 6 (CMIP6) experimental design and organization. Geosci. Model Dev. 9 (5), 1937–1958.

Farneti, R., Downes, S.M., Griffies, S.M., Marsland, S.J., Behrens, E., Bentsen, M., Bi, D., Biastoch, A., Boening, C., Bozec, A., et al., 2015. An assessment of Antarctic circumpolar current and Southern Ocean meridional overturning circulation during 1958–2007 in a suite of interannual CORE-II simulations. Ocean Model. 93, 84–120.

Friedrich, H., Levitus, S., 1972. An approximation to the equation of state for sea water, suitable for numerical ocean models. J. Phys. Oceanogr. 2 (4), 514–517.

Gent, P.R., Mcwilliams, J.C., 1990. Isopycnal mixing in ocean circulation models. J. Phys. Oceanogr. 20 (1), 150–155.

Golaz, J.-C., Caldwell, P.M., Van Roekel, L.P., Petersen, M.R., Tang, Q., Wolfe, J.D., Abeshu, G., Anantharaj, V., Asay-Davis, X.S., Bader, D.C., et al., 2019. The DOE E3SM coupled model version 1: Overview and evaluation at standard resolution. J. Adv. Modelling Earth Syst. 11 (7), 2089–2129.

Griffies, S.M., Biastoch, A., Böning, C., Bryan, F., Danabasoglu, G., Chassignet, E.P., England, M.H., Gerdes, R., Haak, H., Hallberg, R.W., et al., 2009. Coordinated ocean-ice reference experiments (COREs). Ocean Model. 26 (1–2), 1–46.

Griffies, S.M., Danabasoglu, G., Durack, P.J., Adcroft, A.J., Balaji, V., Böning, C.W., Chassignet, E.P., Curchitser, E., Deshayes, J., Drange, H., et al., 2016. OMIP contribution to CMIP6: Experimental and diagnostic protocol for the physical component of the ocean model intercomparison project. Geosci. Model Dev. 9 (9), 3231–3296.

Griffies, S.M., Yin, J., Durack, P.J., Goddard, P., Bates, S.C., Behrens, E., Bentsen, M., Bi, D., Biastoch, A., Böning, C.W., et al., 2014. An assessment of global and regional sea level for years 1993–2007 in a suite of interannual CORE-II simulations. Ocean Model. 78, 35–89.

Held, I., Guo, H., Adcroft, A., Dunne, J., Horowitz, L., Krasting, J., Shevliakova, E., Winton, M., Zhao, M., Bushuk, M., et al., 2019. Structure and performance of GFDL's CM4. 0 climate model. J. Adv. Modelling Earth Syst. 11 (11), 3691–3727.

Hemer, M.A., Katzfey, J., Trenham, C.E., 2013. Global dynamical projections of surface ocean wave climate for a future high greenhouse gas emission scenario. Ocean Model. 70, 221–245.

Hsu, C.-W., Yin, J., Griffies, S.M., Dussin, R., 2021. A mechanistic analysis of tropical Pacific dynamic sea level in GFDL-OM4 under OMIP-I and OMIP-II forcings. Geosci. Model Dev. 14 (5), 2471–2502.

Hunke, E.C., Lipscomb, W.H., Turner, A., Jeffery, N., Elliott, S., 2008. CICE: The Los Alamos sea ice model, documentation and software user's manual. T-3 Fluid Dynamics Group, Los Alamos National Laboratory, Los Alamos, NM 87545.

Jayne, S.R., 2009. The impact of abyssal mixing parameterizations in an ocean general circulation model. J. Phys. Oceanogr. 39 (7), 1756–1775.

Josey, S.A., Hirschi, J.J.-M., Sinha, B., Duchez, A., Grist, J.P., Marsh, R., 2018. The recent Atlantic cold anomaly: Causes, consequences, and related phenomena. Annu. Rev. Mar. Sci. 10, 475–501.

Kistler, R., Kalnay, E., Collins, W., Saha, S., White, G., Woollen, J., Chelliah, M., Ebisuzaki, W., Kanamitsu, M., Kousky, V., et al., 2001. The NCEP–NCAR 50-year reanalysis: Monthly means CD-ROM and documentation. Bull. Am. Meteorol. Soc. 82 (2), 247–268.

Kobayashi, S., Ota, Y., Harada, Y., Ebita, A., Moriya, M., Onoda, H., Onogi, K., Kamahori, H., Kobayashi, C., Endo, H., et al., 2015. The JRA-55 reanalysis: General specifications and basic characteristics. J. Meteorol. Soc. Jpn. Ser. II 93 (1), 5–48.

Large, W.G., McWilliams, J.C., Doney, S.C., 1994. Oceanic vertical mixing: A review and a model with a nonlocal boundary layer parameterization. Rev. Geophys. 32 (4), 363–403.

Large, W., Yeager, S.G., 2009. The global climatology of an interannually varying air–sea flux data set. Clim. Dynam. 33 (2–3), 341–364.

Lee, W.-L., Wang, Y.-C., Shiu, C.-J., Tsai, I.-c., Tu, C.-Y., Lan, Y.-Y., Chen, J.-P., Pan, H.-L., Hsu, H.-H., et al., 2020. Taiwan Earth system model version 1: Description and evaluation of mean state. Geosci. Model Dev. 13 (9), 3887–3904.

Li, Y., Liu, H., Ding, M., Lin, P., Yu, Z., Yu, Y., Meng, Y., Li, Y., Jian, X., Jiang, J., et al., 2020. Eddy-resolving simulation of CAS-LICOM3 for phase 2 of the ocean model intercomparison project. Adv. Atmospheric Sci. 37 (10), 1067–1080.

Lin, P., Yu, Z., Liu, H., Yu, Y., Li, Y., Jiang, J., Xue, W., Chen, K., Yang, Q., Zhao, B., et al., 2020. LICOM model datasets for the CMIP6 ocean model intercomparison project. Adv. Atmospheric Sci. 37 (3), 239–249.

Locarnini, R., Mishonov, A., Antonov, J., Boyer, T., Garcia, H., Baranova, O., Zweng, M., Paver, C., Reagan, J., Johnson, D., et al., 2013. World Ocean Atlas 2013. In: Temperature, vol. 1, NOAA Atlas NESDIS 73.

Marsh, R., 2000. Recent variability of the North Atlantic thermohaline circulation inferred from surface heat and freshwater fluxes. J. Clim. 13 (18), 3239–3260.

McCarthy, G.D., Smeed, D.A., Johns, W.E., Frajka-Williams, E., Moat, B.I., Rayner, D., Baringer, M.O., Meinen, C.S., Collins, J., Bryden, H.L., 2015. Measuring the Atlantic meridional overturning circulation at 26 N. Prog. Oceanogr. 130, 91–111.

Moat, B.I., Smeed, D.A., Frajka-Williams, E., Desbruyères, D.G., Beaulieu, C., Johns, W.E., Rayner, D., Sanchez-Franks, A., Baringer, M.O., Volkov, D., et al., 2020. Pending recovery in the strength of the meridional overturning circulation at 26 ° N. Ocean Sci. 16 (4), 863–874.

Rayner, N., Parker, D.E., Horton, E., Folland, C.K., Alexander, L.V., Rowell, D., Kent, E.C., Kaplan, A., 2003. Global analyses of sea surface temperature, sea ice, and night marine air temperature since the late nineteenth century. J. Geophys. Res.: Atmos. 108 (D14).

Redi, M.H., 1982. Oceanic isopycnal mixing by coordinate rotation. J. Phys. Oceanogr. 12 (10), 1154–1158.

Schmitt, R.W., Bogden, P.S., Dorman, C.E., 1989. Evaporation minus precipitation and density fluxes for the North Atlantic. J. Phys. Oceanogr. 19 (9), 1208–1221.

Shi, J.-R., Talley, L.D., Xie, S.-P., Peng, Q., Liu, W., 2021. Ocean warming and accelerating Southern Ocean zonal flow. Nature Clim. Change 11 (12), 1090–1097.

Sidorenko, D., Rackow, T., Jung, T., Semmler, T., Barbi, D., Danilov, S., Dethloff, K., Dorn, W., Fieg, K., Gößling, H.F., et al., 2015. Towards multi-resolution global climate modeling with ECHAM6–FESOM. Part I: Model formulation and mean climate. Clim. Dynam. 44 (3–4), 757–780.

Smeed, D.A., Josey, S., Beaulieu, C., Johns, W.E., Moat, B.I., Frajka-Williams, E., Rayner, D., Meinen, C.S., Baringer, M.O., Bryden, H.L., et al., 2018. The North Atlantic Ocean is in a state of reduced overturning. Geophys. Res. Lett. 45 (3), 1527–1533.

St. Laurent, L., Garrett, C., 2002. The role of internal tides in mixing the deep ocean. J. Phys. Oceanogr. 32 (10), 2882–2899.

Stammer, D., Köhl, A., Vlasenko, A., Matei, I., Lunkeit, F., Schubert, S., 2018. A pilot climate sensitivity study using the CEN coupled adjoint model (CESAM). J. Clim. 31 (5), 2031–2056.

Steele, M., Morley, R., Ermold, W., 2001. PHC: A global ocean hydrography with a high-quality Arctic Ocean. J. Clim. 14 (9), 2079–2087.

Sun, Z., Small, J., Bryan, F., Tseng, Y.-h., Liu, H., Lin, P., 2021. The impact of wind corrections and ocean-current influence on wind stress forcing on the modeling of pacific north equatorial countercurrent. Ocean Model. 166, 101876.

Taboada, F.G., Stock, C.A., Griffies, S.M., Dunne, J., John, J.G., Small, R.J., Tsujino, H., 2019. Surface winds from atmospheric reanalysis lead to contrasting oceanic forcing and coastal upwelling patterns. Ocean Model. 133, 79–111.

Tseng, Y.-h., Bryan, F.O., Whitney, M.M., 2016a. Impacts of the representation of riverine freshwater input in the community earth system model. Ocean Model. 105, 71–86.

Tseng, Y.-H., Chien, M.-H., 2011. Parallel domain-decomposed Taiwan multi-scale community ocean model (PD-TIMCOM). Comput. & Fluids 45 (1), 77–83.

Tseng, Y.-H., Dietrich, D.E., 2006. Entrainment and transport in idealized three-dimensional gravity current simulation. J. Atmos. Ocean. Technol. 23 (9), 1249–1269.

Tseng, Y.-h., Lin, H., Chen, H.-c., Thompson, K., Bentsen, M., Böning, C.W., Bozec, A., Cassou, C., Chassignet, E., Chow, C.H., et al., 2016b. A North and Equatorial Pacific ocean circulation in the CORE-II hindcast simulations. Ocean Model. 104, 143–170.

Tseng, Y.-H., Shen, M.-L., Jan, S., Dietrich, D.E., Chiang, C.-P., 2012. Validation of the kuroshio current system in the dual-domain Pacific ocean model framework. Prog. Oceanogr. 105, 102–124.

Tsujino, H., Urakawa, L.S., Griffies, S.M., Danabasoglu, G., Adcroft, A.J., Amaral, A.E., Arsouze, T., Bentsen, M., Bernardello, R., Böning, C.W., et al., 2020. Evaluation of global ocean–sea-ice model simulations based on the experimental protocols of the ocean model intercomparison project phase 2 (OMIP-2). Geosci. Model Dev. 13 (8), 3643–3708.

Tsujino, H., Urakawa, S., Nakano, H., Small, R.J., Kim, W.M., Yeager, S.G., Danabasoglu, G., Suzuki, T., Bamber, J.L., Bentsen, M., et al., 2018. JRA-55 based surface dataset for driving ocean–sea-ice models (JRA55-do). Ocean Model. 130, 79–139.

Colin de Verdière, A., Ollitrault, M., 2016. A direct determination of the World Ocean barotropic circulation. J. Phys. Oceanogr. 46 (1), 255–273.

Weijer, W., Cheng, W., Garuba, O.A., Hu, A., Nadiga, B., 2020. CMIP6 models predict significant 21st century decline of the Atlantic meridional overturning circulation. Geophys. Res. Lett. 47 (12), e2019GL086075.

van Westen, R.M., Dijkstra, H.A., 2021. Ocean eddies strongly affect global mean sea-level projections. Sci. Adv. 7 (15), eabf1674.

Williams, P.D., 2009. A proposed modification to the Robert–Asselin time filter. Mon. Weather Rev. 137 (8), 2538–2546.

Young, C.-C., Liang, Y.-C., Tseng, Y.-H., Chow, C.-H., 2014. Characteristics of the RAW-filtered leapfrog time-stepping scheme in the ocean general circulation model. Mon. Weather Rev. 142 (1), 434–447.

Young, C.-C., Tseng, Y.-H., Shen, M.-L., Liang, Y.-C., Chen, M.-H., Chien, C.-H., 2012. Software development of the TaIwan multi-scale community ocean model (TIMCOM). Environ. Model. Softw. 38, 214–219.

Zheng, Y., Giese, B.S., 2009. Ocean heat transport in simple ocean data assimilation: Structure and mechanisms. J. Geophys. Res. Oceans 114 (C11).

Zweng, M., Reagan, J., Antonov, J., Locarnini, R., Mishonov, A., Boyer, T., et al., 2013. World Ocean Atlas 2013. In: Levitus, S., Mishonov, A. (Eds.), Salinity, vol. 2. NOAA Atlas NESDIS 74, Washington, DC, 39.